A spatial healing metric for wound healing modeling

Ekrem Ekici[1] and Ahmed S. Dalaq[1,2*]

[1]Interdisciplinary Research Center for Biosystems and Machines, King Fahd University of Petroleum & Minerals, Dhahran, Saudi Arabia.
[2]Department of Bioengineering, King Fahd University of Petroleum & Minerals, Dhahran, Saudi Arabia.

*Corresponding author(s). E-mail(s): ahmed.dalaq@kfupm.edu.sa;
Contributing authors: ekrem.ekici@kfupm.edu.sa;

Abstract

We propose a new healing metric for improved tracking of the wound healing process across arbitrary wound geometries. A Fickian diffusion equation with a logistic nonlinear term is solved using the open-source finite element framework FEniCSx. The model is verified and calibrated by comparing finite element simulation results with experimental data from the literature, focused on the circular rabbit ear wound. To address the limitations of fixed-threshold metrics, we introduce a spatial healing metric, $\boldsymbol{\beta}$, which captures the average cell density across the wound domain. This metric reflects healing differences arising from geometry and variations in diffusion and mitotic parameters. Parametric sweeps over the diffusion coefficient–mitotic generation ($\boldsymbol{D}$–$\boldsymbol{s}$) space reveal that different parameter combinations can yield the same healing time but with quite different spatial profiles. We also study multiple wound geometries to validate the applicability of the proposed metric. Our results demonstrate that the proposed $\boldsymbol{\beta}$ metric exposes limitations of the classical threshold-based approach, particularly under conditions of high diffusion and low mitotic generation, where traditional metrics suggest full healing despite spatial discrepancies in cell density.

Keywords: wound healing, finite element method, healing metric, numerical modeling, nonlinear diffusion

This is a post-peer-review, pre-copyedit version of an article accepted for publication in *Biomechanics and Modeling in Mechanobiology*. For online access on Journal's official website, please visit https://doi.org/10.1007/s10237-025-02029-3

1 Introduction

Among the most seminal reports in the field of wound healing, and particularly using a continuum approach, the classical mass balance model considers the wound as a control volume, where cell proliferation and cell growth (mitotic generation) occur at the wound location [1–4]. The edge of the wound (the unwounded part) gradually migrates towards the center of the wound, driven by diffusion mechanism, and proliferating cells reproduce at their current locations via a logistic profile. This model also accounts for contact inhibition, where proliferated cells jam at the wound and thus slow the cell buildup, especially at the center of the wound [1].

Considering a Fickian diffusion with logistic proliferation, the wound healing process depends on two parameters: the diffusion coefficient and the mitotic generation rate along with the wound size. This simple model (i.e. diffusion-mitotic generation [1]) provided the milestone upon which other investigators could build by adding important biological mechanisms, thereby increasing the model's fidelity. Among the first updates to this model was the addition of a chemotactic flux to capture up-gradient migration driven by growth factor concentration [8]. Furthermore, to account for extracellular matrix (ECM) remodeling [9, 10], a three-field model was introduced comprising three partial differential equations representing cell density, ECM density, and growth factor concentration, where their interplay governs the wound healing process [11]. In addition, wounds that extend beyond the epidermal layer involve mechanical and viscoelastic effects during closure and so a string-based models were introduced to capture wound contraction forces [12, 13]. The model was further enhanced by including blood vascularization (angiogenesis) [14–16], inflammation and debris clearance [17], and even endogenous bioelectric fields [18, 18]. One of the first finite element models proposed in [19]. The transport of oxygen and growth factors of epidermal cells are coupled and the model predicted the total healing time for circular, rectangular and ellipsoidal wounds. This model is further extended to model dermal wound contraction [16], angiogenesis and wound closure [20, 21], and surgical wounds [22] by adding several new parameters.

While these additions represent major advancements in wound healing modeling, they introduce new parameters that are often phenomenological in nature. Each of these parameters requires calibration and a proven and justified link to experimentally measured data [19, 21, 23]. To this end, chemical, localized mechanical, spatial/structural, and electrical measurements must be monitored in real time for healing wounds. Nevertheless, the current literature is quite scarce in such data, as most datasets are limited to wound radius or healing percentage over time (Fig. 1), along with image snapshots of wounds from mainly animal models and some human subjects [6, 24–26]. In addition, random motility of cells, growth factor signaling, small-scale traction forces, and ECM effects may, to some extent, be lumped into the diffusion term and the rate of mitotic generation introduced in Ref [1].

Therefore, in this work, we revisit the seminal model in [1], applied a finite element scheme to enable multidimensional analysis, and optimize its computational performance. We aim to capture the kinematics of wound healing, that is, the deformations and rates at which the wound and its boundaries close during the healing process. This kinematics are, in essence, the manifestation of underlying wound dynamics that

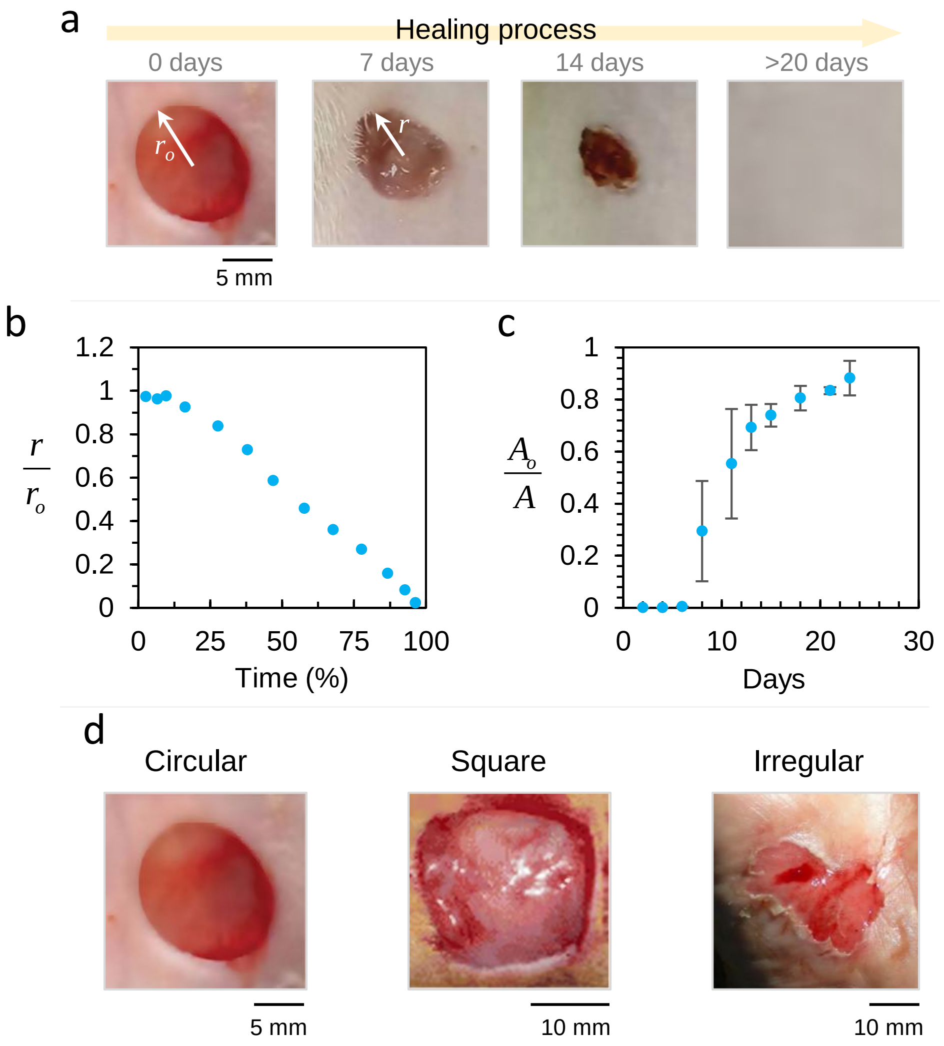

Fig. 1: (a) Wound healing progression in a rat animal study over 0–20 days (adapted from [5]). (b) Wound radius over time in an ear wound rabbit case (data are adapted from [1]), showed a tracking ratio suitable for circular wounds. (c) Wound area reduction ratio, ideal for irregular wounds (data are for a square wound in a rat subject, adapted from [6]). (d) Different wound geometries, including: circular (adapted from [5]), square (adapted from [6]), and irregular (adapted from [7]).

have been the focus of earlier, more mechanistic models (e.g., models of vascularization [14–16], ECM remodeling [9, 10], growth factor signaling [8, 11], and contractile forces [12, 13]). Since most available wound-healing datasets are limited to observational snapshots (e.g., wound area or radius over time) [6, 24–26], they are particularly suited for calibrating kinematic wound-healing models based on diffusion–mitosis processes. Being a single PDE with only a few parameters lends itself naturally to the finite element scheme, making the model tractable for extension to arbitrary 2D and 3D wound morphologies. Moreover, this diffusion-mitotic generation model admits closed-form solutions in simple 1D Cartesian and axisymmetric cases [27], allowing two-way verification of numerical simulations before proceeding to full fledge parametric or calibration studies.

To this end, we aim to demonstrate how a finite element approach, relying on a minimal number of parameters, can simulate wound healing in circular, square, and irregular wounds, as well as in arbitrary 3D wound morphologies, while remaining compatible with the simplicity and limited experimental data in the literature. In addition, models often adopted either a radius cut-off or a cell density threshold to represent a healed state [1, 14, 28]. Both approaches, however, fail to account for the actual spatial distribution of the wound healing across the wound domain. That is an aspect that becomes critical for irregular, sharp-edged wounds (slits) and is especially important for 3D wound models. To address this limitation, we also propose a new spatial healing metric that is representative of spatial wound recovery over time.

In Sec. 2, we derive the finite element system that represents the cell diffusion and proliferation. We derive the weak formulation and discuss relevant boundary conditions. We include implementation details of the nonlinear solver and present the model calibration of the solver. In Sec. 3, we verify the nonlinear solver considering the well-studied rabbit wound. We compare the findings with [1] and we present the calibration of the parameters to match experimental data in [29].

In Sec. 4, we analyze the effect of parameter p that adjusts the nonlinearity of the diffusion. Moreover, we discuss the varying contact inhibition of the cells and effect of these of the unwounded cell distributions. Based on the findings so far, we then introduce the new metric in Sec. 5 and discuss its applicability on different types/sizes/geometries of wounds in Sec. 6. Lastly, we present the conclusions and future work in Sec. 7. In Appendix A, we present a verification case for the FEM code using analytical model from [27]. We also show the mesh and timestep convergences studies in Appendix B and detailed model calibration setup in Appendix C.

2 Methodology

2.1 Nonlinear diffusion equation

We solve the diffusion equation to model the cell activity over the wound domain. A nonlinear logistic term is included in diffusion equation to take the proliferation into account [1, 30, 31]:

$$\frac{\partial \phi}{\partial t} = D[\nabla \cdot (\phi/\phi_0)^p \nabla \phi] + s\phi(1 - \phi/\phi_0) \quad \text{in } \Omega, \tag{1}$$

where ϕ is the cell density, t is the time, ϕ_0 is the unwounded cell density, p is an integer that sets Fickian ($p = 0$) or non-fickian diffusion ($p > 0$), D is the diffusion coefficient, and s is the proliferation/mitotic generation rate of the cells in the domain Ω.

2.2 Weak formulation

We use finite element method (FEM) to obtain cell activity on spatial wound domain. Thus, we require an FEM discretization of (1) and its boundary conditions. We solve a time dependent PDE so it requires time derivative discretization. For simplicity, we define $f = s\phi(1-\phi/\phi_0)$ and $q(\phi) = (\phi/\phi_0)^p$ for now, and we resubstitute them at the end of the weak form derivation. We define a time level n and write

$$\left(\frac{\partial \phi}{\partial t}\right)^{n+1} = D[\nabla \cdot q(\phi^{n+1})]\nabla \phi^{n+1} + f^{n+1}. \tag{2}$$

We can use finite differences to approximate time derivative:

$$\left(\frac{\partial \phi}{\partial t}\right)^{n+1} \approx \frac{\phi^{n+1} - \phi^n}{\Delta t}, \tag{3}$$

where Δt is the time step. At time level $t = n + 1$, we write backward Euler discretization of (1):

$$\frac{\phi^{n+1} - \phi^n}{\Delta t} = D[\nabla \cdot q(\phi^{n+1})\nabla \phi^{n+1}] + f^{n+1}. \tag{4}$$

We now multiply the terms in (4) with test function v and integrate the terms over the wound domain Ω:

$$\int_\Omega \frac{\phi^{n+1} - \phi^n}{\Delta t} v = \int_\Omega D[\nabla \cdot q(\phi^{n+1})\nabla \phi^{n+1}]v + \int_\Omega f^{n+1} v. \tag{5}$$

We apply product rule for the contents of the first term for the right hand side in (5):

$$D[\nabla \cdot q(\phi^{n+1}\nabla \phi^{n+1}]v = D\nabla \cdot [q(\phi^{n+1})\nabla \phi^{n+1} v] + Dq(\phi^{n+1})\nabla \phi^{n+1}\nabla v. \tag{6}$$

With the divergence theorem, the volume integral of the first term in (6) converts to boundary integral:

$$\int_\Omega D\nabla \cdot [q(\phi^{n+1})\nabla \phi^{n+1} v]dx = \int_{\partial\Omega} D(q(\phi^{n+1})\nabla \phi^{n+1} v \cdot \hat{n} dS). \tag{7}$$

where $\hat{n}$ denotes the outward normal vector for the boundary. If we apply Dirichlet (ϕ=ϕ_D) condition, terms in (7) become zero. Then we substitute (7) into (5):

$$\int_\Omega \frac{\phi^{n+1} - \phi^n}{\Delta t} v = \int_\Omega Dq(\phi^{n+1})\nabla \phi^{n+1}\nabla v + \int_\Omega f^{n+1} v. \tag{8}$$

Finally, rearranging terms in (8) and resubstitution of f and $q(\phi^{n+1})$ gives the complete weak formulation of (1) in variational form:

$$F(\phi^{n+1}; v) = \int_\Omega [\phi^{n+1}v - \phi^n v + \Delta t D(\phi^{n+1}/\phi_0)^p \nabla\phi^{n+1}\nabla v - \Delta t s\phi(1-\phi/\phi_0)v]dx = 0. \tag{9}$$

Due to the presence of the logistic term, the finite element solution of (9) is nonlinear regardless of the value of p and it can apply to any geometrical dimension. We note that the del operator ∇ in Eq. (9) is $\nabla = \frac{\partial}{\partial x}\mathbf{i} + \frac{\partial}{\partial y}\mathbf{j} + \frac{\partial}{\partial z}\mathbf{k}$ for cartesian grid and $\nabla = \frac{\partial}{\partial r}\mathbf{e}_r + \frac{1}{r}\frac{\partial}{\partial\theta}\mathbf{e}_\theta + \frac{\partial}{\partial z}\mathbf{e}_z$ for cylindrical grid with corresponding unit vectors. In the calibration (Appendix C) and verification (Sec. 3) sections, we consider cylindrical coordinates, then Eq. (9) becomes:

$$F(\phi^{n+1}; v) = \int_\Omega [\phi^{n+1}v - \phi^n v + \Delta t D(\phi^{n+1}/\phi_0)^p \frac{\partial\phi^{n+1}}{\partial r}\frac{\partial v}{\partial r} - \Delta t s\phi(1-\phi/\phi_0)v]rdr = 0. \tag{10}$$

where r denotes the radial component of the cylindrical domain.

2.3 Initial and boundary conditions

For Eq. (1), the initial condition for all the cases is identical, the cell density on the wound edge is set to one and zero elsewhere. We use Dirichlet and Neumann boundary conditions (BCs) to model diffusion process in this paper. Dirichlet BC states that there is a constant cell density on the boundary $\partial\Omega_D$:

$$\phi = \phi_D \quad \text{on } \partial\Omega_D, \tag{11}$$

where ϕ_D is the specified cell density. Neumann boundary implies a constant flux on the boundary $\partial\Omega_N$ in the normal direction:

$$D\frac{\partial\phi}{\partial n} = g \quad \text{on } \partial\Omega_N, \tag{12}$$

where g is the specified concentration flux. If g is equals to zero, that means that the boundary is impermeable and cells accumulate over time. We present the numerical setups for 1D radial wound and 2D circular, rectangular and irregular wound shapes in Fig. 2. For the 1D cases, we use a Dirichlet boundary on the wound edge, $\phi_D(r_o, t) = 1$ and we impose symmetry boundary condition at the wound center, as the surface integral vanishes with $r \longrightarrow 0$ assuming cylindrical domain (Fig. 2a). For 2D cases, we set a cartesian grid and impose Dirichlet boundaries on the wound edges (Fig. 2b,c).

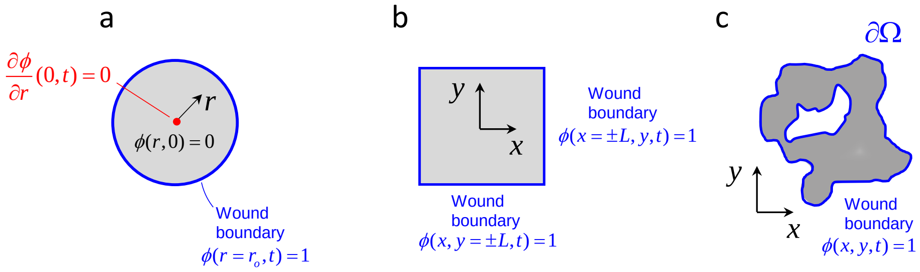

Fig. 2: Boundary conditions for (a) circular, (b) rectangular and (c) irregular wound domains. Blue borders represent the wound edges where unwounded cell density is 1.0.

2.4 Nonlinear solver

We implement a nonlinear FEM code to solve Eq. (10) with the Newton solver and present the implementation details in this section.

2.4.1 Open-source framework

We use the open-source FEM framework, FEniCSx project [32] that provides a framework for solving partial differential equations (PDEs) with the finite element method (FEM). It incorporates efficient kernels for matrix assembly to accelerate solution times. Users define the PDE's weak form using the high-level Unified Form Language (UFL) [33] within a Python interface. The FEniCSx Form Compiler (FFCx) [34] processes these UFL definitions to generate optimized low-level C code for local tensor computations. DOLFINx then uses this code to assemble the global system. The resulting compiled forms can be represented as sparse matrices, which can be formatted using the Portable Extensible Toolkit for Scientific Computation (PETSc) [35] via its Python binding, petsc4py [36].

2.4.2 Newton solver

As we seek for nonlinear solutions, we implement a Newton solver using Newton's method. This method relies on initial guess and converges to the solution in incremental steps. We use a Krylov subspace method and preconditioners (KSP) to construct solver object. We set Generalized Minimal Residual (GMRES) in KSP object and use boomeramg preconditioner from hypre preconditioning library [37]. We converge to the solution in incremental steps with the relative tolerance of $1E-8$. We present the mesh and timestep convergence studies in Appendix B.

3 Wound healing model and verification

As a first measure, we introduce the healing metric presented in [1]. According to this healing criterion, when the cell density in any finite element reaches 80%, the wound is considered healed for the entire wound. For the circular wound (i.e., axisymmetric 1D model), the minimum $\phi_{\min}$ is at the center ($r = 0$) at any time instant, t. The total healing time, t_h, is therefore computed by tracking the time taken for the cell density at the wound center to reach 0.8. For non-circular wounds, such as square or irregular wound domains, we track the minimum $\phi_{\min}$ and identify the instant t at which: $\phi_{\min} \geq 0.8$, which marks the moment the wound is considered healed. Fig. 3a shows the wound radius, r, over time for actual experiments on a rabbit ear wound (with an initial radius, $r_0 = 0.517$ cm), indicated as square blue markers from [29]. The 1D FEM model is then run using the respective diffusion coefficient and calibrated mitotic generation rate (Appendix C): ($D = 7.2 \times 10^{-6}$ cm^2 / h, $s = 0.0314$ 1/ h) that captures the experimental data. We consider the Fickian diffusion by setting $p = 0$ and we set $\phi_0 = 1.0$ (i.e., non-chronic wounds) in FEM calculations. As such, the FEM scheme captures both the experimental values and the trend quite well. In particular, the FEM matched the healing time of the experiment: $t_h = 599$ hours. We present a analytical verification case in Appendix A and more detailed calibration steps in Appendix C.

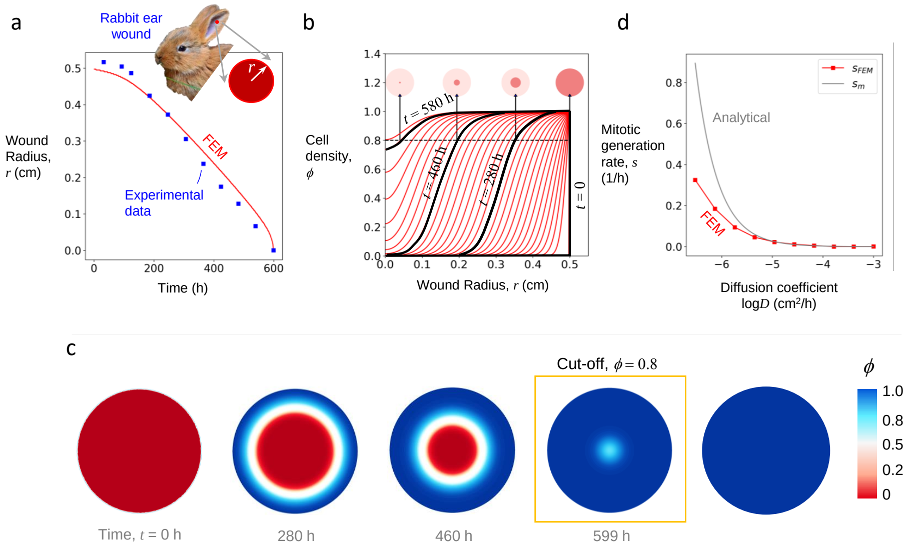

Fig. 3: Model verification data for the rabbit ear wound. (a) FEM model calibrated for the radius–time profile of the rabbit ear wound case. The inset of the rabit is adapted from [38]. (b) FEM prediction of cell density, ϕ, progression across the wound radius $0 < r < r_0$ at different times ($t = 0$ to $t = t_h = 600$ h). Black curves indicate selected checkpoints at $t = 0$, 280, 460, and 480 h, highlighting the kinematic evolution of the healing process. (c) Illustration of the wound healing front progressively closing in to heal the wound. (d) Comparison of FEM results of mitotic generation rate with the analytical prediction from the Maini equation against $\log D$.

In addition to wound kinetics, we tracked the density of wound cells along the wound radius from $r_0 > r > 0$, and plotted its profile at different time points on

Fig. 3b. The wound heals progressively from right to left towards the center of the wound, $r = 0$. At the start ($t = 0$), the wound is a cavity and thus unhealed everywhere: $\phi = 0$ throughout the domain except at its boundary ($r = r_0$), where $\phi = 1$. With the passage of time, ϕ progressively increases from right to left until most of the wound reaches $\phi > 0.8$. A dotted black line is shown in the same plot to indicate the instant at which the wound is considered healed (i.e., when $\phi > 0.8$). We have highlighted three checkpoints: $t = 0$, 280, 460, and 580 hours, with the corresponding wound shapes displayed above each orange-highlighted line. Fig. 3c presents a zoomed-out view of the wound at these time checkpoints to demonstrate the kinematics of the healing process in a circular wound (see Supplementary video: Circular). Clearly, based on both Fig. 3b and Fig. 3c, the wound center is the last region to start healing. Even when the wound is considered healed, 20% of the wound at $r = 0$ remains unhealed. The solver, however, requires a relatively long time to asymptotically reach the fully healed state, where $\phi(r = 0) = 1$. Hence, a cutoff is applied to yield a reasonable healing time, t_h. After running the solver for an extremely long time, we achieve an almost completely homogeneous contour map of the wound (i.e., fully blue, for $t > 599$ h on Fig. 3c).

So far, the FEM model is capable of generating the healing time, t_h, as a function of the diffusion coefficient and mitotic rate: $t_h = f(D, s)$. While healing time is easily measurable, the FEM can achieve the same healing duration, say $t_h = 599$ hours as in the rabbit case [1], using different combinations of (D, s). Thus, the (D, s) design space corresponding to a given t_h that matches experimental data is non-unique. However, there exists a reasonable range of diffusion coefficients, $D = 10^{-7}$–10^{-3} cm^2/h (or 10^{-11}–10^{-7} cm^2/s), for which a corresponding s value can be calibrated. We use the golden section search (Appendix C) algorithm to find the corresponding s values for varied D (Fig. 3c). In other words, Fig. 3c shows the different possible combinations of (D, s) that satisfy the healing time t_h of the rabbit case. Ref. [1] actually proposes a fixed value of D, and thus a single corresponding s is found, which also matches the healing time $t_h = 599$ hours, as indicated by a square marker. Now, a third layer of verification of the FEM model is to compare its D–s plot for $t_h = 599$ h with expression from literature. We verify our FEM output for (D, s) for a specific t_h, by comparing the FEM results (in red) against the relation for s_m proposed by Maini in [31]:

$$s_m = \frac{v^2}{4D\,\ln 2} \tag{13}$$

where v is the healing speed in cm/h and D is the diffusion coefficient in cm^2/h. This analytical model assumes a circular wound and is a fitted expression derived from a numerical solution (i.e., empirical-analytical fit). We present the comparison between s_{FEM} and s_m in Fig. 3d. For proper comparison, the healing speed v for the rabbit case was adopted from [1], corresponding to the same healing time $t_h = 599$ h of the FEM results (shown in red). The diffusivity D is varied, and its respective s values are computed using both the FEM and the analytical relation then plotted accordingly. Clearly, the FEM results show good agreement with the analytical values due to calibration, and they successfully capture the overall trend. This agreement verifies the FEM model against the known analytical expression of Maini [31]. The divergent trend of the s values for the diffusion coefficients is smaller than 10^{-6} because of the lack of data that have been used to obtain Eq. 13 in [31]. In addition to this limitation, Eq. 13 can indeed be used to estimate the D–s relationship, but only if the healing speed v is known, either through direct experiments or numerical modeling as in here or simple numerical approach of [1].

4 Effect of contact inhibition, p

In its most generic form, the FEM model can compute the healing time as a function of multiple parameters: $t_h = f(D, s, p, \phi_0)$. The variation in D–s has been introduced above, and ϕ_0 is set to $\phi_0 = 1$, throughout the manuscript to allow full wound healing (i.e., no chronic wounds). The parameter p is a critical value that modulates cell diffusion toward the wound domain. When $p > 0$, cells are capable of migrating more rapidly in crowded regions, while $p = 0$ assumes a purely Fickian diffusion model, that implies no contact inhibition due to cell crowding at the wound site. Fig. 4a, b and c show respectively the wound density contour maps for a circular wound at the healed state (i.e., $\phi = 0.8$) for $p = 0$, 2, and 4. The even values of p are chosen arbitrarily, simply to demonstrate a noticeable effect of increasing p on the contour maps. Overall, increasing p has a strong influence on prolonging the healing time t_h. We also observe that the wound healing front becomes sharper with higher p values. Consequently, the wound center exhibits different levels of healing even when the cutoff criterion ($\phi = 0.8$) is applied uniformly across all p cases. This closer examination of the role of p reveals that the cutoff commonly adopted in the literature, and used here, is not a fully accurate representation of healing. There is, therefore, a need for a spatially resolved representation of wound healing that accounts for the distribution of cell density ϕ across the wound domain. Throughout this work, however, we assume the Fickian case ($p = 0$) for the wound model.

5 A metric for spatial healing, β

Motivated by the observations in Sec. 4, even though the same cutoff $\phi = 0.8$ was applied, different spatial distributions of ϕ were observed (Fig. 3). These are leading to varied levels of spatial healing, therefore we recognize a limitation in relying on a fixed threshold for ϕ. Since the FEM scheme described here is not restricted to 1D but is also applicable to 2D (including complex, irregular shapes) and even 3D wound topologies, this spatial discrepancy in ϕ becomes increasingly problematic. We are therefore in need of a spatial healing metric that is general and applicable across 1D, 2D, and 3D domains (denoted by Ω and having a volume V). To address this, we propose to average the cell density ϕ across the wound domain, which we define as β:

$$\beta = \frac{\int_\Omega \phi dV}{\int_\Omega dV}. \tag{14}$$

The cases shown in this manuscript are primarily 1D or 2D and, therefore, the averaging is performed over area rather than volume (i.e., the integral is taken over dA). Having $\beta = 1$ indicates a fully healed wound, meaning that every point across the wound domain has reached $\phi = 1$. In contrast, $\beta \longrightarrow 0$ implies a completely unhealed (open) wound.

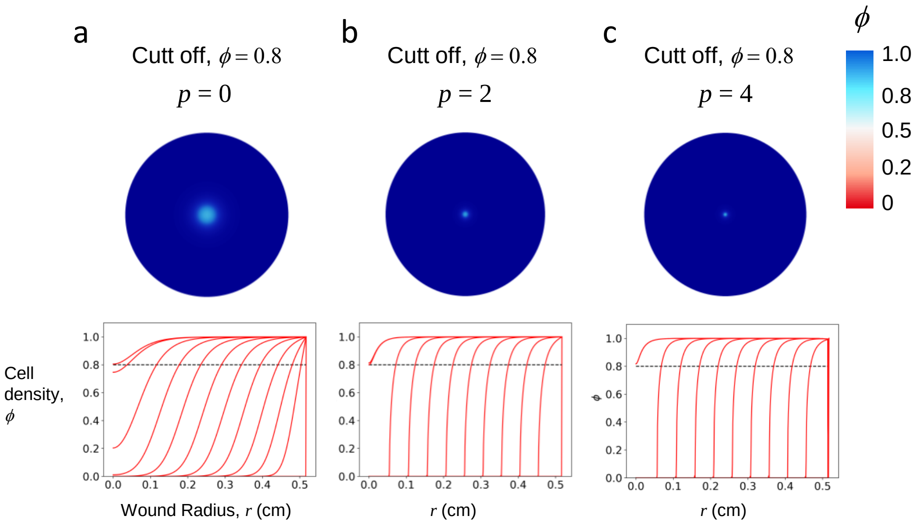

Fig. 4: Unwounded cell distributions for varying p considering the circular rabbit wound. The mitotic generation s and diffusion coeffecient D are fixed to observe the effect of p on cell distribution and total healing time. The corresponding total healing times are 599 h, 2181 h and 3628 h for $p = 0$, $p = 2$ and $p = 4$ respectively. For these cases, $r_0 = 0.517$ cm, $D = 7.6 \times 10^{-6}$ cm^2/h and $\Delta t = 1$ h.

To demonstrate the necessity of the spatial healing metric β, we ran the model for two different circular wound cases: (i) the rabbit ear wound ($r_0 = 0.517$ cm) from [1], and (Fig 5a) (ii) an additional rat wound case ($r_0 = 0.75$ cm) from [26] (Fig 5b). Considering the classic healing state cut-off $\phi(0, t) \geq 0.8$, the FEM model was used to conduct a full factorial parameter sweep over the D–s space for their respective wound sizes and reported healing times: $t_h = 599$ h for the rabbit case and $t_h = 336$ h for the rat case. We performed the parameter sweep over $D = [7.6 \times 10^{-6}, 10^{-3}]$ cm^2/h and the corresponding $s = [0.01, 0.09]$ 1/h to evaluate our proposed spatial healing metric $\beta = f(D, s)$, shown in Fig. 5a and Fig.5b. Both figures use a fixed β range for the color bar and contour limits. In these sweeps, we ignored the effects of p and ϕ_o to isolate the impact of D and s.

Importantly and interestingly, variation in the β contour map, ranging from $\beta =$ 0.88 to 0.999, is observed despite using the same healing state cutoff of $\phi = 0.8$. In light of the "healing front" described by Fisher [3], the healing efficacy is governed by the ratio D/s.

An increase in D causes β to drop from 0.99 to 0.88 (a decrease of approximately 11%) under the same cutoff criterion. In contrast, increasing s tends to increase β at any fixed value of D, since higher proliferation increases ϕ throughout the wound domain, producing a more uniform distribution and yielding higher values of β (up to $\beta \approx 0.999$), particularly at low D. In other words, at low D and high s, cell proliferation dominates but is not strongly supported by migration. However, because the wound front advances slowly while mitotic generation remains high, ϕ accumulate

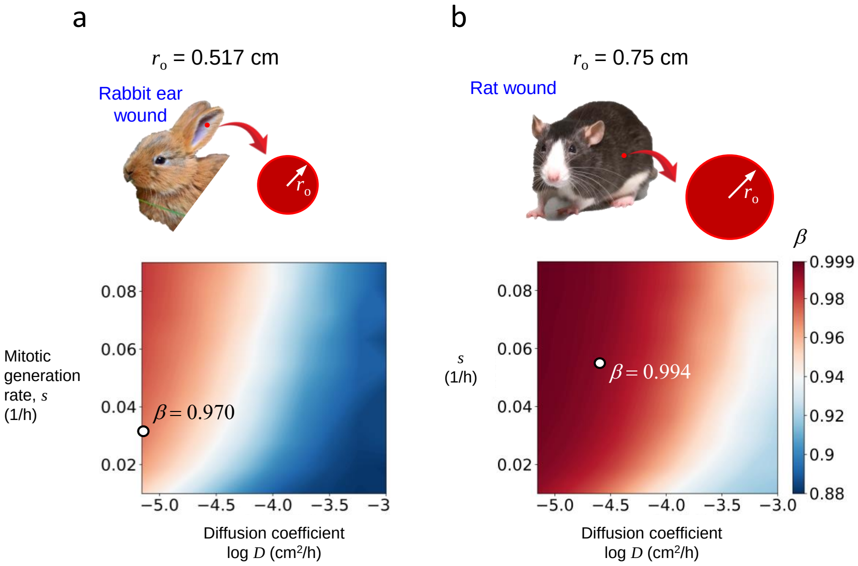

Fig. 5: Averaged cell density, β, distributions for varying $D - s$ for (a) rabbit ear and (adapted from [38] (b) rat wounds (adapted from [39]).

almost uniformly behind the healing front, giving the appearance of a uniformly healed wound. These high β values are typically reached only after longer healing durations and therefore correspond to larger total healing times t_h. Conversely low β (poor spatial healing) requires less healing time, t_h.

In contrast, for high D (that is, a rapidly advancing healing front) and low s, the wound front becomes sharp, and most cell accumulation occurs near the rim of the wound. This leads to significant spatial disparity and a lower average β (e.g., $\beta = 0.88$), despite satisfying the same threshold-based healing criterion. Such low β values are typically achieved over shorter healing times t_h.

For a given isoline on the (D, s, β) surface, an increase in D must be accompanied by a corresponding increase in s to preserve a uniform spatial distribution of ϕ. At high s and low D, a sharp peak of cells may form near the wound center and decay gradually toward the front, whereas at high D and low s, the wound edge advances faster than proliferation can replenish cells, resulting in a thin leading front and thickened rims. Thus, maintaining a constant value of β requires that both D and s increase together (following geometrically increasing contour isolines inure 5), preserving a balanced migration–proliferation dynamics. This trend contrasts with the healing-time surface $t_h(D, s)$ (Fig. 3), where multiple (D, s) combinations can yield the same t_h. In that case, a shorter healing time can result from either a higher s or higher D, as one parameter can compensate for the other. However, such combinations do not necessarily correspond to the same spatial healing uniformity in ϕ.

The two cases (rabbit ear and rat wound) also have proposed representative mitotic generation rates for their respective wounds [31, 40]. Using these values, the corresponding diffusion coefficients D were computed inversely via the golden section search algorithm (as discussed earlier in Appendix C). These specific (D, s) points are denoted as circular markers on the contour plots. Notably, they exhibit significantly different β values (e.g., $\beta = 0.970$, 0.994) despite applying the same healing cutoff ($\phi = 0.8$), which was assumed to indicate that both have completed healing. In reality, however, these two cases reflect different levels of healing, as revealed by their distinct β values. This clearly shows that the assumption of complete healing based on a fixed cutoff is not appropriate. Instead, the proposed metric β may be more accurate and more spatially representative measure of healing.

6 Case study: Circular, square and irregular wound

In this section, we demonstrate how to use the proposed FEM model for different case studies: (i) a 0.75 cm circular rat wound [26] (Fig. 6a), (ii) a 2×2 cm square rat wound [6] (Fig. 6b), and (iii) a 9.11 cm^2 irregular wound with the additional challenge of having an uninjured island at the center [41] (Fig. 6c) (refer to the supplementary material for raw coordinates). These figures show the kinematic progression of wound healing over time using calibrated (D, s) combinations and the standard cutoff ($\phi = 0.8$). See Supplementary videos: Circular, square and irregular. We set $\Delta t = 2\text{h}$ for 2D cases in order to accelerate convergence. The model successfully captures the gradual healing process from the periphery, regardless of how irregular the shape may be, and shows how the wound progressively heals toward a single point. This convergence point, where the wound fronts meet, is geometry-dependent. For symmetric shapes like the circular and square wounds, it occurs at the center (i.e., $r = 0$ or $(x = 0, y = 0)$). In contrast, for irregular shapes, the final healing point can be anywhere across the domain—typically where it is farthest from the wound periphery (where $\phi = 1$) and vise versa. For example, the narrow region in the irregular wound case, indicated by the white arrow in Fig. 6c, is one of the first areas to heal, as the opposing wound edges are closest in proximity and require the shortest distance to close.

Recall that the FEM model can now readily generate the healing time as a function of parameters: $t_h = f(D, s)$. For each of the case studies, we show the corresponding D–s parameter space and the resulting t_h as a contour map (Figs 6a,d; 6b,e; and 6c,f). We also superimpose a black curve on each of these maps, representing the calibrated (D, s) combinations that capture the experimentally observed healing time in each case (i, ii, iii). This iso-line (constant t_h) represents all combinations of (D, s) that produce the same healing time, and analysts can move along it to explore different possible diffusion–mitosis interactions that still match the observed wound healing behavior. A single localized measurement of either D or s can then be used to pinpoint a representative (D, s) pair along this iso-line. In other words, by taking known diffusion coefficient values from the literature, we can identify a corresponding point on the iso-line that accurately represents the wound healing process for that specific case. This highlights that wound healing for a given t_h can be achieved through different

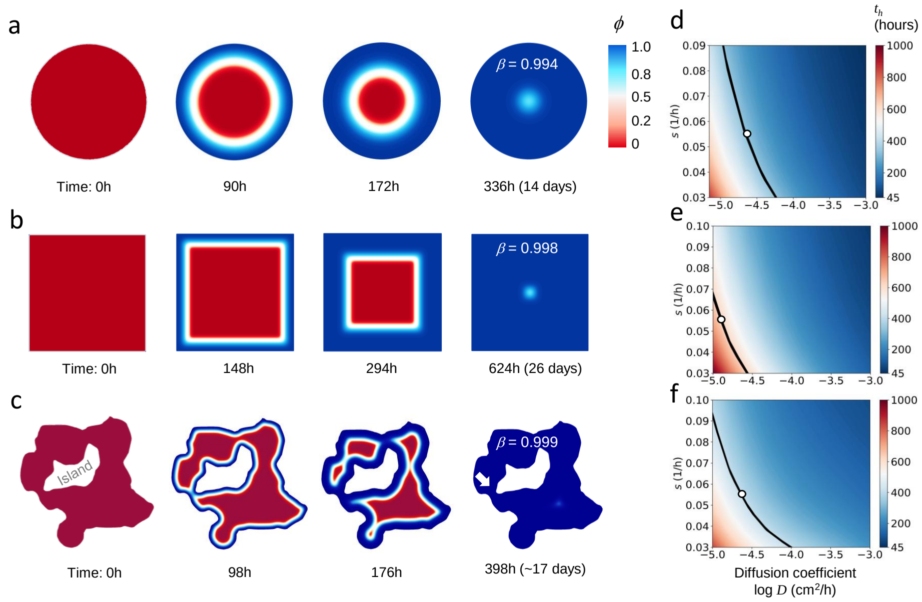

Fig. 6: 2D healing process in different time checkpoints for (a) circular, (b) rectangular and (c) irregular shaped wounds. The D-s clusters for the circular (d) and (f) irregular wounds share the same reference point (denoted as while circle with black border) with $D = 2.42$ cm^2/h and $s = 0.0\overline{5}$ 1/h while the reference point for rectangular wound has $D = 1.24$ cm^2/h and $s = 0.0\overline{5}$ 1/h.

mechanisms, such as high motility with low mitotic generation, or low motility with high mitotic generation, both resulting in the same overall healing time.

One way to use the FEM framework presented in this paper is to first measure the healing time experimentally and then run the FEM model over a wide range of (D, s) values to generate corresponding t_h results. The measured t_h can then be matched to the iso-line corresponding to that value on the contour plot (similar to the black iso-line shown previously). Next, by estimating either a D or s value, one can pinpoint a representative (D, s) values along the iso-line. Interestingly, the wound healing process may be compromised due to either low motility (low D) or low mitotic activity (low s), and these contour maps allow analysts to visualize and analyze both of these distinct diagnostic scenarios.

7 Conclusion

In this paper, we propose a new spatial healing metric that numerically represents the healing progress for any 1D, 2D, or 3D representation of wounds. Our first test case involved a circular wound model for a rabbit ear. For numerical computations, we built a framework using finite element method. The FEM was used to solve a Fickian diffusion equation augmented with a logistic nonlinear term to simulate the wound healing process as a function of diffusion coefficient D, mitotic generation rate s, and cell contact inhibition modulated by the parameter p. In most cases, p was fixed, representing the Fickian assumption. We implemented the nonlinear diffusion solver using the open-source FEniCSx framework and its supporting components. Before conducting parametric studies, we validated the FEM against experimental results from the rabbit ear wound and verified it using the analytical relation proposed by Maini. The FEM model was thus able to capture both the kinetics and kinematics of the wound healing process.

We carried out a study on contact inhibition of cells, modulated by the parameter p, which was found to slow down the healing process for higher ps, sharpen the healing front. This reveals how using a single cutoff threshold to define a healed state may not be accurate. Different values of p resulted in varying levels of healing at the wound center, even when the same cutoff threshold was applied. To address this, we introduced a spatial healing metric, β, that captures the distribution of healing across the wound domain. This metric proved to be sensitive to wound geometry as well as D and s values, even under the same cutoff. This insight became particularly clear when comparing different experimental cases: the rabbit wound versus the rat wound, which produced contrasting β values despite having the same cutoff threshold.

Utilizing the power and tunability of the nonlinear solver developed in this work, we carried out a full-factorial parametric sweep over the (D, s) space for three different wound geometries: circular, rectangular, and irregularly shaped wounds, each calibrated using experimental healing times. As expected, higher diffusion and mitotic generation rates led to faster healing times. However, we demonstrated the limitations of the classic healing metric, as varying (D, s) combinations produced different β values despite using the same ϕ cutoff for the healed state. Most importantly, we showed the effectiveness of the proposed spatial metric, β, in capturing healing progression across non-regular wound shapes. This metric provides a more accurate and geometry-sensitive representation of wound healing compared to traditional cutoff-based methods. The FEM model enables mapping of (D, s) combinations via iso-lines on contour plots. Given a known healing time, the corresponding iso-line can be identified. Then, by estimating either D or s, a representative model can be selected. Moving along the iso-line helps determine whether impaired healing is due to reduced cell motility or limited mitotic activity, which offers a valuable diagnostic tool.

In future work, we aim to extend this framework to simulate 3D non-regular wound shapes using the implemented nonlinear solver. Additionally, a one-way coupled diffusion model will be developed to explore interactions between healing agents and epidermal wounds.

Supplementary information. The geometry data of the irregular wound for skin island and outer boundaries are provided as supplementary material.

Acknowledgements. This work was supported by the interdisciplinary research center (IRC): Biosystems and Machines at King Fahd University of Petroleum & Minerals (KFUPM). Authors acknowledge Fatma Mousa Alzamel for providing the wound healing data for the circular and rectangular wounds. Ekrem Ekici gratefully acknowledges funding for his postgraduate studies from Türkiye's Ministry of National Education.

Declarations

Conflict of interest

The authors declare no competing interests.

Ethics declarations

The authors declare that they do not have any financial or personal relationships with other people or organisations.

Code availability

The implemented solver can be provided upon reasonable request.

Author contributions

EE—model generation, data generation, analysis, solver implementation; manuscript writing. ASD—conceptualization; data analysis and interpretation; manuscript writing.

Appendix A Solver verification

We verify the solver using an analytical solution proposed by [27];

$$u(x,t) = \beta \left[\exp\left(\ln\left(1 + \frac{u_0}{\beta}\right) \exp(-\beta t) \cos\left(\sqrt{1+\beta} x\right)\right) - 1\right], 0 < x < \frac{\pi}{2\sqrt{1+\beta}}. \tag{A1}$$

Eq. A1 hold for certain spatially varying diffusivity field

$$D(u) = \frac{\beta}{u+\beta},$$

and mitotic generation term

$$R(u) = \beta(1-u)\ln(1+\frac{u}{\beta}),$$

in corresponding Fisher-KPP equation:

$$\frac{\partial u}{\partial t} = \frac{\partial}{\partial x}\left(D(u)\frac{\partial u}{\partial x}\right) + R(u). \tag{A2}$$

As indicated in [27], we impose $u(x, o)$ of Eq. (A1) as an initial condition in our code with $\beta = 1$. Solving this system in cartesian coordinates gives the results shown in Fig. A1. The FEM results show agreement against the analytical solution proposed by [27].

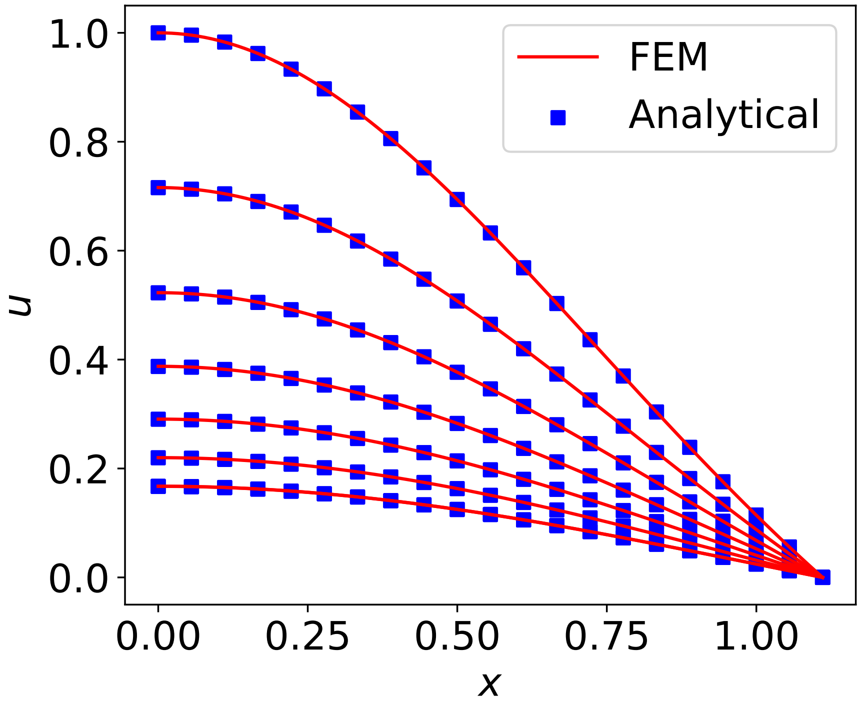

Fig. A1: Comparison of the results between our FEM code and [27] for $\beta = 1$.

Appendix B Mesh and timestep convergence

We perform mesh and time-step convergence studies in order to settle the mesh size and time-step parameters for finite element calculations. We use the rabbit wound as a convergence case. The convergence results are shown in Fig. B2. Using more than 120 elements stops changing the total healing time (Fig. B2a) so we use more than 120 degree 1 continuous Galerkin finite elements for the 1D radial domain. This indicates that cell size specified as $\Delta x < r/80$. Inspecting Fig. B2b, time steps smaller than $\Delta t \leq 2$ show negligible differences and we set the time step to be $\Delta t = 1$ h for 1D case and $\Delta t = 2$ for 2D cases.

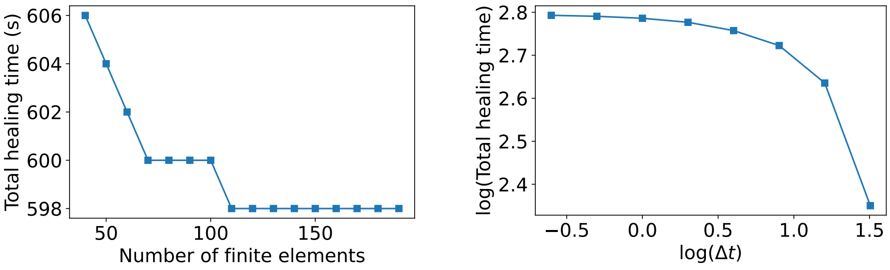

(a)

(b)

Fig. B2: (a) mesh and (b) timestep convergence plots for the benchmark case. The timesteps values are decreasing geometrically starting from 32 h and ending at 0.25 h.

Appendix C Model calibration for (D,s)

We verify our nonlinear solver based on the data presented in [1] and [29]. The healing period of the wound on the rabbit ear is studied. We pick the Fickian diffusion case where $p = 0$. We generate the 1D radial domain such that $r = 0$ implies the center of the wound and $r = r_0$ implies the edge of the wound where cell density is 1.0 (unwounded). For calculating the wound healing distribution, number of elements in 1D domain is $N = 200$, timestep is $\Delta t = 1$h, the diffusivity coefficient is $D = 7.2 \times 10^{-6}$ cm^2/h and mitotic rate is $s = 0.0288$ 1/h. We take the initial radius of the wound as $r_0 = 0.5$ cm and healing speed is measured as 0.0207 cm/day [29]. We then solve the (10). Imposing the Dirichlet boundary condition on $r = L_0$ gives the initial condition of the wounded domain. Unwounded cells start to spread and increase towards $r = 0$ from $r = r_0$ based on the parameters D and s. At the center of the wound $(r = 0)$, we apply Neumann boundary condition for allowing cell density to accumulate up to 1.0. As n_0 indicates the unwounded cell density, it is a vector that contains cell density of 1.0 over the domain (we assume that wound will be completely healed). We calculate the total healing time as 611.0 hours using FEM. This shows that the results of FEM calculations agree very well with the total healing time 599 hours in [1]. We further optimize the mitotic rate, s, to match the total healing time of 599 hours for constant $D = 7.2 \times 10^{-6}$ cm^2/h. We also change the radius of the wound as $r_0 = 0.517$ cm to match the experimental data in [29]. We use the golden section algorithm to find s within the designated interval. The optimized mitotic rate for this case is calculated as $s_{opt} = 0.031418$ /h, giving total healing time of 599 h, which compares very well with the experimental data (Fig. 3a).

References

[1] Sherratt, J.A., Murray, J.D.: Models of epidermal wound healing. Proceedings of the Royal Society of London. Series B: Biological Sciences **241**(1300), 29–36 (1990) https://doi.org/10.1098/rspb.1990.0061

[2] Dale, P.D., Maini, P.K., Sherratt, J.A.: Mathematical modeling of corneal epithelial wound healing. Mathematical biosciences **124**(2), 127–147 (1994) https://doi.org/10.1016/0025-5564(94)90040-x

[3] Fisher, R.A.: The Wave of Advance of Advantageous Genes. Annals of Eugenics **7**(4), 355–369 (1937) https://doi.org/10.1111/j.1469-1809.1937.tb02153.x . _eprint: https://onlinelibrary.wiley.com/doi/pdf/10.1111/j.1469-1809.1937.tb02153.x

[4] Kolmogorov, A.: Étude de l'équation de la diffusion avec croissance de la quantité de matière et son application à un problème biologigue. Pages: 1 Publication Title: Moscow Univ. Bull. Ser. Internat. Sect. A Volume: 1 (1937). https://cir.nii.ac.jp/crid/1370004235502855043

[5] Li, J., , C. Haiyan, , L. Lei, , L. Hao, , Cui, Z.: Wound healing activity of neferine in experimental diabetic rats through the inhibition of inflammatory cytokines and nrf-2 pathway. Artificial Cells, Nanomedicine, and Biotechnology **48**(1), 96–106 (2020) https://doi.org/10.1080/21691401.2019.1699814 . Publisher: Taylor & Francis _eprint: https://doi.org/10.1080/21691401.2019.1699814

[6] Giusto, G., Vercelli, C., Comino, F., Caramello, V., Tursi, M., Gandini, M.: A new, easy-to-make pectin-honey hydrogel enhances wound healing in rats. BMC complementary and alternative medicine **17**, 1–7 (2017) https://doi.org/10.1186/s12906-017-1769-1

[7] Doug, B.: Bicycle injury - Hand Abrasion, Day 1. Page Version ID: 1270842421 (2012). https://en.wikipedia.org/w/index.php?title=Wound&oldid=1270842421

[8] Wearing, H.J., Sherratt, J.A.: Keratinocyte growth factor signalling: a mathematical model of dermal–epidermal interaction in epidermal wound healing. Mathematical Biosciences **165**(1), 41–62 (2000) https://doi.org/10.1016/S0025-5564(00)00008-0

[9] Schiller, M., Javelaud, D., Mauviel, A.: TGF-beta-induced SMAD signaling and gene regulation: consequences for extracellular matrix remodeling and wound healing. Journal of Dermatological Science **35**(2), 83–92 (2004) https://doi.org/10.1016/j.jdermsci.2003.12.006

[10] Menon, S.N., Flegg, J.A.: Mathematical Modeling Can Advance Wound Healing Research. Advances in Wound Care **10**(6), 328–344 (2021) https://doi.org/10.1089/wound.2019.1132

[11] Maggelakis, S.A.: A mathematical model of tissue replacement during epidermal wound healing. Applied Mathematical Modelling **27**(3), 189–196 (2003) https://doi.org/10.1016/S0307-904X(02)00100-2

[12] Arciero, J.C., Mi, Q., Branca, M.F., Hackam, D.J., Swigon, D.: Continuum model of collective cell migration in wound healing and colony expansion. Biophysical Journal **100**(3), 535–543 (2011) https://doi.org/10.1016/j.bpj.2010.11.083

[13] Pozzi, G., Ciarletta, P.: Geometric control by active mechanics of epithelial gap closure. Soft Matter **20**(4), 900–908 (2024) https://doi.org/10.1039/D3SM01419C . Publisher: Royal Society of Chemistry

[14] Vermolen, F.J., Javierre, E.: A finite-element model for healing of cutaneous wounds combining contraction, angiogenesis and closure. Journal of Mathematical Biology **65**(5), 967–996 (2012) https://doi.org/10.1007/s00285-011-0487-4

[15] Pettet, G.J., Byrne, H.M., Mcelwain, D.L.S., Norbury, J.: A model of wound-healing angiogenesis in soft tissue. Mathematical Biosciences **136**(1), 35–63 (1996) https://doi.org/10.1016/0025-5564(96)00044-2

[16] Vermolen, F., Javierre, E.: Computer simulations from a finite-element model for wound contraction and closure. Journal of Tissue Viability **19**(2), 43–53 (2010) https://doi.org/10.1016/j.jtv.2009.11.003

[17] Dunster, J.L., Byrne, H.M., King, J.R.: The Resolution of Inflammation: A Mathematical Model of Neutrophil and Macrophage Interactions. Bulletin of Mathematical Biology **76**(8), 1953–1980 (2014) https://doi.org/10.1007/s11538-014-9987-x

[18] Reid, B., Zhao, M.: The Electrical Response to Injury: Molecular Mechanisms and Wound Healing. Advances in wound care **3**, 184–201 (2014) https://doi.org/10.1089/wound.2013.0442

[19] Vermolen, F.J., Adam, J.A.: A finite element model for epidermal wound healing. In: Computational Science–ICCS 2007: 7th International Conference, Beijing, China, May 27-30, 2007, Proceedings, Part I 7, pp. 70–77 (2007). https://doi.org/10.1007/978-3-540-72584-8_10 . Springer

[20] Flynn, C.: Finite element models of wound closure. Journal of tissue viability **19**(4), 137–149 (2010) https://doi.org/10.1016/j.jtv.2009.10.001

[21] Vermolen, F., Javierre, E.: A finite-element model for healing of cutaneous wounds combining contraction, angiogenesis and closure. Journal of mathematical biology **65**, 967–996 (2012) https://doi.org/10.1007/s00285-011-0487-4

[22] Valero, C., Javierre, E., García-Aznar, J., Gómez-Benito, M.: Nonlinear finite element simulations of injuries with free boundaries: application to surgical wounds.

International journal for numerical methods in biomedical engineering **30**(6), 616–633 (2014) https://doi.org/10.1002/cnm.2621

[23] Vermolen, F.J., Javierre, E.: A Suite of Continuum Models for Different Aspects in Wound Healing. In: Gefen, A. (ed.) Bioengineering Research of Chronic Wounds: A Multidisciplinary Study Approach, pp. 127–168. Springer, Berlin, Heidelberg (2009). https://doi.org/10.1007/978-3-642-00534-3_6 . https://doi.org/10.1007/978-3-642-00534-3_6

[24] Parella, K., Moody, K., Wortel, D., Colegrove, H., Elser, J.A.: HOXA3 accelerates wound healing in diabetic and aged non-diabetic mammals. Scientific Reports **13**(1), 9923 (2023) https://doi.org/10.1038/s41598-023-36933-4 . Publisher: Nature Publishing Group

[25] Zimny, S., Schatz, H., Pfohl, M.: The Effects of Ulcer Size on the Wound Radius Reductions and Healing Times in Neuropathic Diabetic Foot Ulcers. Experimental and Clinical Endocrinology & Diabetes **112**, 191–194 (2004) https://doi.org/10.1055/s-2004-817932 . Publisher: J. A. Barth Verlag in Georg Thieme Verlag KG Stuttgart · New York

[26] Hu, X., Xu, H., Bu, L., Sun, J., Deng, J., Song, K., Wang, L., Pang, B.: Exploring the wound healing potential of dietary nitrate in diabetic rat model. Frontiers in Physiology **15**, 1475375 (2024) https://doi.org/10.3389/fphys.2024.1475375

[27] McCue, S.W., Bradshaw-Hajek, B.H., Simpson, M.J.: Exact time-dependent solutions of a fisher–kpp-like equation obtained with nonclassical symmetry analysis. Applied Mathematics Letters **132**, 108151 (2022) https://doi.org/10.1016/j.aml.2022.108151

[28] Sherratt, J.A.: Cellular growth control and travelling waves of cancer. SIAM Journal on Applied Mathematics **53**(6), 1713–1730 (1993) https://doi.org/10.1137/0153079

[29] Brenk, H.: Studies in restorative growth processes in mammalian wound healing. Journal of British Surgery **43**(181), 525–550 (1956) https://doi.org/10.1002/bjs.18004318115

[30] Tremel, A., Cai, A., Tirtaatmadja, N., Hughes, B.D., Stevens, G.W., Landman, K.A., O'Connor, A.J.: Cell migration and proliferation during monolayer formation and wound healing. Chemical Engineering Science **64**(2), 247–253 (2009) https://doi.org/10.1016/j.ces.2008.10.008

[31] Maini, P.K., McElwain, D.S., Leavesley, D.: Travelling waves in a wound healing assay. Applied Mathematics Letters **17**(5), 575–580 (2004) https://doi.org/10.1016/S0893-9659(04)90128-0

[32] Barrata, I.A., Dean, J.P., Dokken, J.S., Habera, M., Hale, J., Richardson, C.,

Rognes, M.E., Scroggs, M.W., Sime, N., Wells, G.N.: DOLFINx: The next generation FEniCS problem solving environment (2023) https://doi.org/10.5281/zenodo.10447666

[33] Alnæs, M.S.: UFL: a finite element form language. In: Automated Solution of Differential Equations by the Finite Element Method: The FEniCS Book, pp. 303–338. Springer, Berlin, Heidelberg (2012). https://doi.org/10.1007/978-3-642-23099-8_17

[34] Logg, A., Ølgaard, K.B., Rognes, M.E., Wells, G.N.: FFC: the FEniCS form compiler. Automated Solution of Differential Equations by the Finite Element Method: The FEniCS Book, 227–238 (2012) https://doi.org/10.1007/978-3-642-23099-8_11

[35] Balay, S., Abhyankar, S., Adams, M.F., Brown, J., Brune, P., Buschelman, K., Dalcin, L., Dener, A., Eijkhout, V., Gropp, W., Karpeyev, D., Kaushik, D., Knepley, M., May, D., McInnes, L.C., Mills, R., Munson, T., Rupp, K., Sanan, P., Smith, B., Zampini, S., Zhang, H., Zhang, H.: PETSc Users Manual (Rev. 3.13) (2020) https://doi.org/10.2172/1614847

[36] Dalcin, L.D., Paz, R.R., Kler, P.A., Cosimo, A.: Parallel distributed computing using python. Advances in Water Resources **34**(9), 1124–1139 (2011) https://doi.org/10.1016/j.advwatres.2011.04.013

[37] Falgout, R.D., Yang, U.M.: hypre: A library of high performance preconditioners. In: International Conference on Computational Science, pp. 632–641 (2002). https://doi.org/10.1007/3-540-47789-6_66 . Springer

[38] Pikrepo: Royalty free rabbit photos | Pikrepo (2025). https://www.pikrepo.com/en/search?q=rabbit

[39] AlexK100: English: A pet fancy rat: black? standard blaze (2007). https://commons.wikimedia.org/wiki/File:Fancy_rat_blaze.jpg

[40] Hjelle, J.T., Golinska, B.T., Waters, D.C., Steidley, K.R., McCarroll, D.R., Dobbie, J.W.: Isolation and propagation in vitro of peritoneal mesothelial cells. Peritoneal Dialysis International **9**(4), 341–347 (1989) https://doi.org/10.1177/089686088900900423

[41] Cardinal, M., Eisenbud, D.E., Armstrong, D.G.: Wound shape geometry measurements correlate to eventual wound healing. Wound repair and regeneration **17**(2), 173–178 (2009) https://doi.org/10.1111/j.1524-475x.2009.00464.x